Angewandte Chemie
Eine Zeitschrift der Gesellschaft Deutscher Chemiker

Supporting Information

Carbene-Catalyzed Activation of Remote Nitrogen Atoms of (Benz)imidazole-Derived Aldimines for Enantioselective Synthesis of Heterocycles

Xing Yang[+], Yongtao Xie[+], Jun Xu, Shichao Ren, Bivas Mondal, Liejin Zhou, Weiyi Tian, Xinglong Zhang,* Lin Hao, Zhichao Jin, and Yonggui Robin Chi**

anie_202016506_sm_miscellaneous_information.pdf

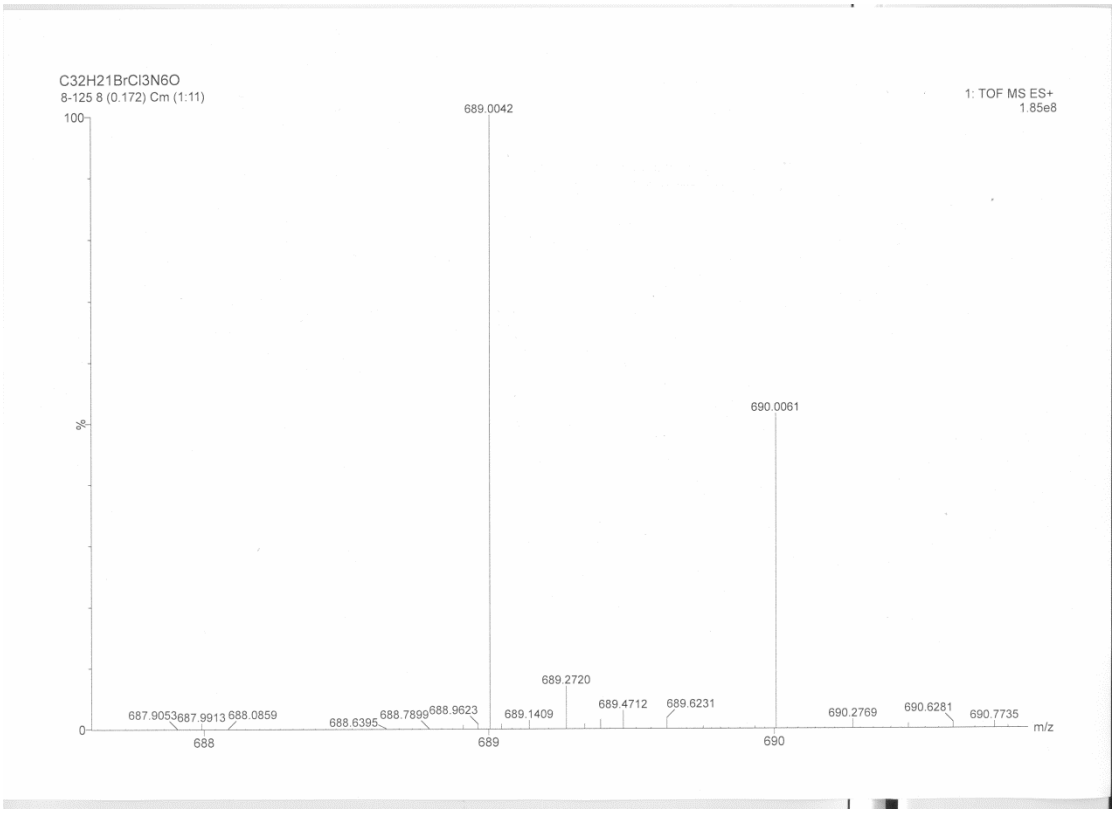

Figure S-2. The HRMS data of intermediate III

Computational methods for mechanism studies

Geometry optimizations in the gas phase were initially carried out using the GFN1-xTB method[2] as implemented in Entos Qcore Version 0.7.[3] The resulting structures were further optimized using global hybrid functional M06-2X[4] with Karlsruhe-family basis set of double-ζ valence def2-SVP[5,6] for all atoms as implemented in *Gaussian 16* rev. A.03.[7] Minima and transition structures on the potential energy surface (PES) were confirmed as such by harmonic frequency analysis, showing respectively zero and one imaginary frequency, at the same level of theory. Intrinsic reaction coordinate (IRC) analyses[8,9] were performed to confirm that the found TSs connect to the right reactants and products.

Single point (SP) corrections were performed using M06-2X functional and def2-TZVP[1] basis set for all atoms. The implicit SMD continuum solvation model[10] was used to account for the solvent effect of dichloromethane (DCM) on the overall free energy PES. Gibbs energies were evaluated at the room temperature, as was used in the experiments, using a quasi-RRHO treatment of vibrational entropies.[11,12]

Vibrational entropies of frequencies below 100 cm^{-1} were obtained according to a free rotor description, using a smooth damping function to interpolate between the two limiting descriptions. The free energies were further corrected using standard concentration of 1 mol/L, which was used in solvation calculations. SMD(DCM)-M06-2X/def2-TZVP//M06-2X/def2-SVP Gibbs energies are given and quoted in kcal mol^{-1} throughout. *Unless otherwise stated, these solvent-corrected values are used for discussion throughout the main text and in this supporting information.*

Non-covalent interactions (NCIs) were analyzed using NCIPLOT[13] calculations. The *.wfn* files for NCIPLOT were generated at M06-2X/DGDZVP[14,15] level of theory. NCI indices calculated with NCIPLOT were visualized at a gradient isosurface value of *s = 0.5* au. These are colored according to the sign of the second eigenvalue (λ_2) of the Laplacian of the density ($\nabla^2\rho$) over the range of –0.1 (blue = attractive) to +0.1 (red = repulsive). Molecular orbitals are visualized using an isosurface value of 0.05 au throughout. All molecular structures and molecular orbitals were visualized using *PyMOL* software.[16]

Distortion-interaction[17,18]/activation strain (DI–AS) model[18-22] is applied to key TSs to discern the factors affecting stereoselectivity. Geometries are taken from along the IRC reaction coordinate at 0.15Å interval and single point gas-phase calculations were performed at M06-2x/def2-TZVP level of theory to obtain DI-AS profiles.

Geometries of all optimized structures (in *.xyz* format with their associated energy in Hartrees) are included in a separate folder named *xyz_structures* with an associated readme.txt file. All these data have been deposited with this Supporting Information and uploaded to zenodo.org (DOI: 10.5281/zenodo.4314003).

Results and Discussions

For our computational study, we used substrates **1a** and **2b** as shown in Scheme S-1. Experimentally, product **3b** is formed with a 95% yield and an enantiomeric ratio (er) of 98:2. We studied the three possible pathways from triaza-diene intermediate **III**. In pathway 1, intermediate **III** could undergo a concerted [4+2] cycloaddition to give a cycloadduct from which the carbene catalyst NHC **D** can be regenerated. In pathway 2, a stepwise aminalization/cyclization is anticipated, where first a C–N bond forms between intermediate **III** and isatin substrate **2b**.

This can be followed by a nucleophilic substitution at imine to regenerate the carbene catalyst NHC **D**. For concerted asynchronous reaction mechanism (pathway 3), the second cyclization step follows immediately upon the completion of the first aminalization step without the formation of a stable intermediate. We computationally studied the above pathways and found that a concerted, highly asynchronous reaction mechanism is possible (*vide infra*).

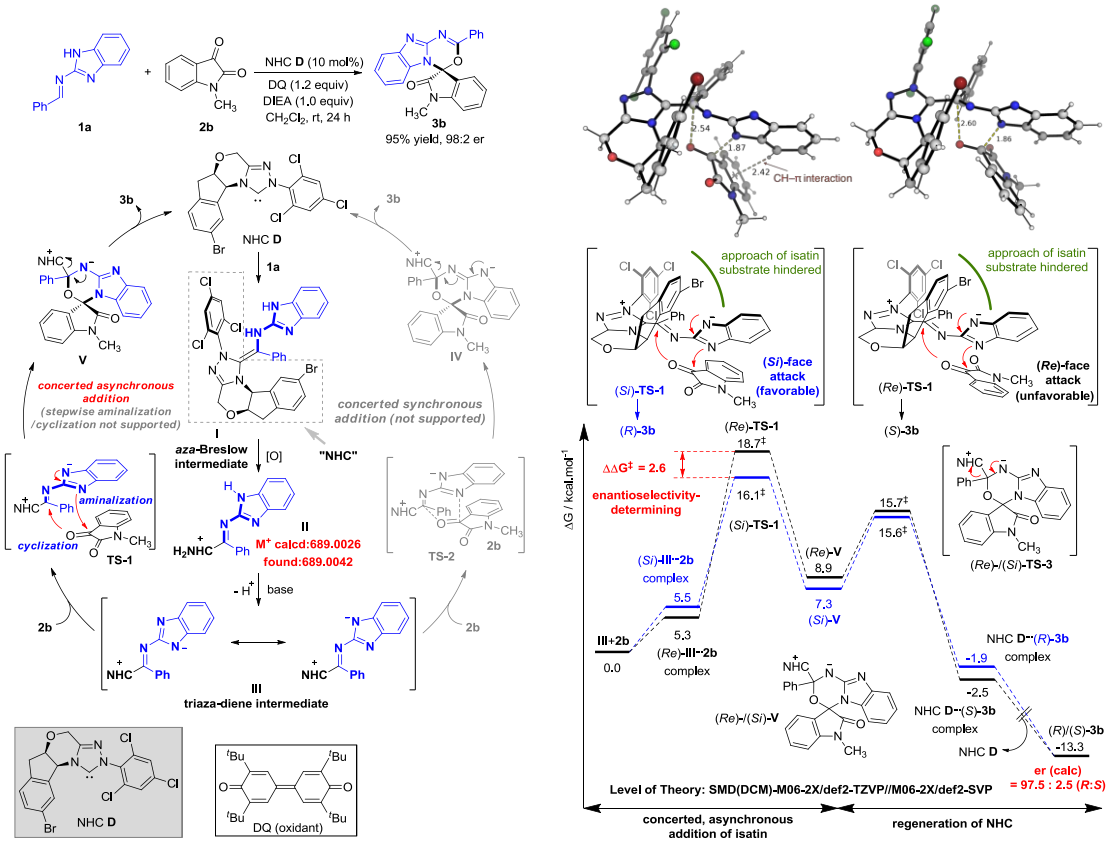

Scheme S-1. Possible pathways for imine functionalization and DFT calculations.

Conformational considerations

To determine the most stable form of the key triaza-diene intermediate (**III**), involved in the reaction mechanism, we performed a thorough conformational sampling. We generated a set of rotamers by performing 5-fold rotations about key dihedral angles as shown in Figure S-3. The generated rotamers were then cleaned by removing those species having overlapping atoms. These were performed using the script in the study of conformational effects on physical-organic descriptors by Brethomé *et al.*[23] A total of 43 resulting rotamers were then subject to geometry optimization using GFN1-xTB in Entos Qcore. The xTB-optimized structures were then clustered to give 3 distinct conformers, which were reoptimized at DFT M06-2X/def2-SVP level. The

resulting structures and their solvent-corrected relative Gibbs energies (SMD(DCM)-M06-2x/def2-TZVP//M06-2x/def2-SVP) are given in Figure S-3. Not surprisingly, the most stable conformer benefits from pi-pi interaction between the phenyl ring on imine substrate (**1a**) and the aryl ring on NHC ligand. The most stable species **III** is used for all subsequent studies.

Chemdraw structure	**DFT optimized conformers of intermediate** III		
III	**III-3b**	**III-3b-2**	**III-3b-3**
	ΔΔG = 0.0	0.7	1.1
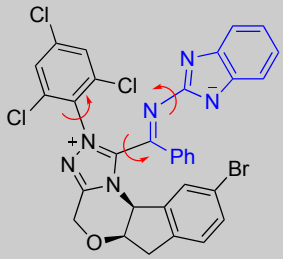	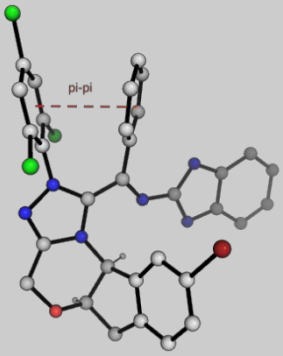	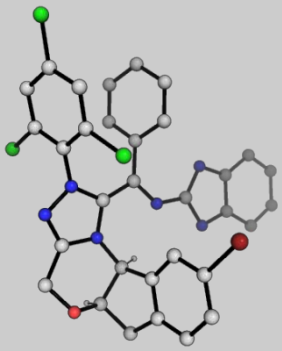	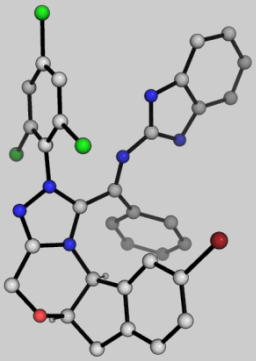

Figure S-3. Chemdraw and DFT optimized conformer structures of key intermediate **III**. Gibbs energy units are given in kcal/mol.

Frontier Molecular Orbitals (FMO) analysis

Figure S-4 shows the frontier molecular orbitals (FMOs) and their associated energies for intermediates **III-3b** (with benzoimidazole protected imine as the substrate) and **III-3ac** (with imidazole protected imine as the substrate) and the isatin substrate **2b** that were used in computation. For the reaction between imine **1b** and isatin **2b** via intermediate **III-3b**, the orbital interaction between the HOMO of **2b** and the LUMO of **III-3b** (HOMO-LUMO gap of 0.203 eV) occurs between the O atom of the ketone group and the C atom of the imine, however, this C–O bond formation does not occur as the TS could not be found computationally. On the other hand, the orbital interaction between HOMO of **III-3b** and LUMO of **2b** has a more compatible orbital interaction and a more favorable HOMO-LUMO gap of 0.176 eV. Thus, the reaction occurs with electrons originating from intermediate **III-3b** and flowing to substrate **2b** (*vide infra*).

Intermediate III-3b	
HOMO	LUMO
-0.24095 eV	-0.07809 eV
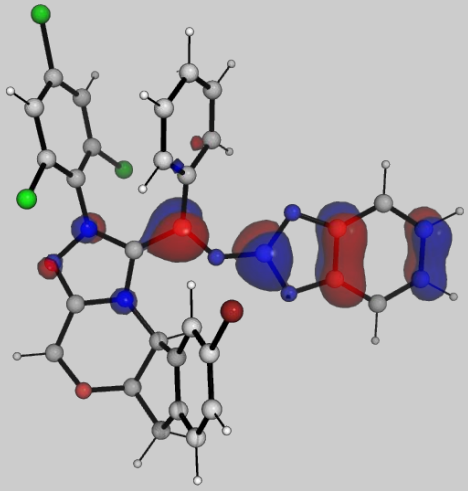	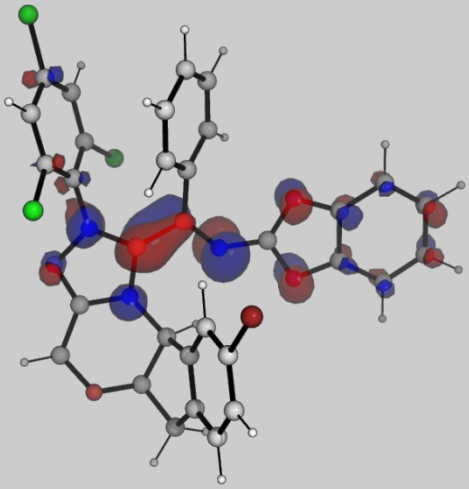
Intermediate III-3ac	
HOMO	LUMO
-0.22152 eV	-0.05259 eV
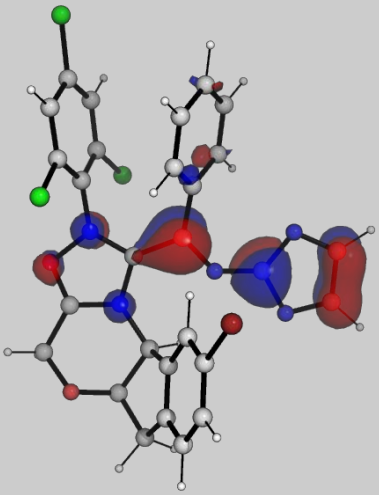	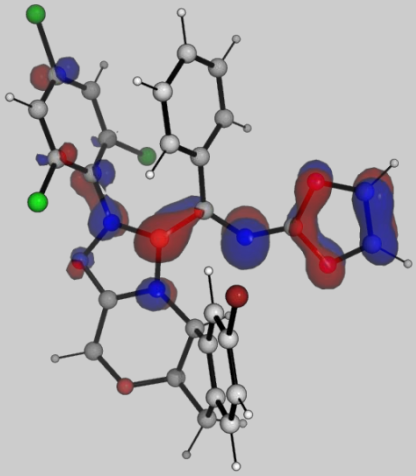
Substrate 2b	
HOMO	LUMO
-0.28085 eV	-0.06494 eV

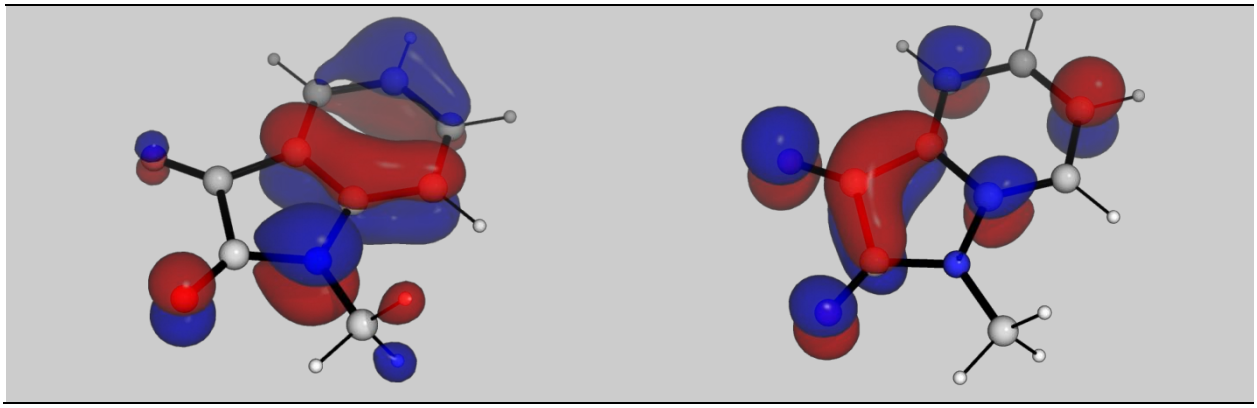

Figure S-4. FMOs, at an isosurface value of 0.05 au, and their associated orbital energies for intermediates **III-3b** and **III-3ac** and substrate **2b**.

The intermediate **III-3ac** arising from the reaction between imine **1ac** (differs from imine **1b** by a lack of additional Ph-ring) and isatin **2b** has similar FMO shapes as intermediate **III-3b**. The orbital interaction between the HOMO of **2b** and the LUMO of **III-3ac** (HOMO-LUMO gap of 0.228 eV) again has less favorable orbital and HOMO-LUMO energy interactions than the orbital interaction between HOMO of **III-3ac** and LUMO of **2b** (a more favorable HOMO-LUMO gap of 0.157 eV). Thus, similarly, the reaction between **III-3ac** and isatin **2b** occurs with electron flowing from the former to the latter.

Reaction between III-3b and 2b

Key transition state (TS) structures

Figure S-5 shows the optimized TS structures for the concerted, highly asynchronous [4+2] cyclo-addition for NHC-catalyzed imine functionalization. These are the stereo-determining TSs. IRC analyses were used to connect these TSs to their respective reactants and products. The reaction is concerted, highly asynchronous as the products resulting from first C–N bond formation optimizes directly to the [4+2]-cycloadducts **Si-/Re-V** (Figure S-5). The bond lengths in these TSs are also suggestive of a concerted, highly asynchronous mechanism: the C–N bond formation occurs at 1.87Å (*Si*-**TS-1**) and 1.86Å (*Re*-**TS-1**), while the C–O bonds are much longer at 2.54Å (*Si*-**TS-1**) and 2.60 Å (*Re*-**TS-1**).

The TS for the addition to the *Si*-face of the isatin substrate, *Si*-**TS-1**, benefits from favorable CH–π interaction between the NHC-activated imine substrate and isatin **2b**. This CH–π interaction is absent in the TS for the addition to the *Re*-face of the isatin substrate, *Re*-**TS-1**. This can be shown by the NCI plots in Figure S-5. Applying DI–AS model to these TSs (Figure S-6), we see that *Si*-**TS-1** has a lower activation barrier than *Re*-**TS-1** due to more favorable interaction energy (in purple), despite having similar strain energy (in blue). Highest occupied molecular orbitals (HOMOs) of both TSs are similar (Figure S-3), suggesting similar electron distribution in these TSs. Thus, the more favorable interaction energy in *Si*-**TS-1** is likely due to more favorable dispersion energy between its fragments. The difference in the Gibb energy of 2.6 kcal mol^{-1} predicts an er of 97.5 : 2.5 in favor of *Si*-face adduct, in excellent agreement with experimental findings (er of 98 : 2).

***Si*-TS-1**	***Re*-TS-1**
$\Delta G^{\ddagger}$ = 16.1 kcal mol^{-1}	$\Delta G^{\ddagger}$ = 18.7 kcal mol^{-1}
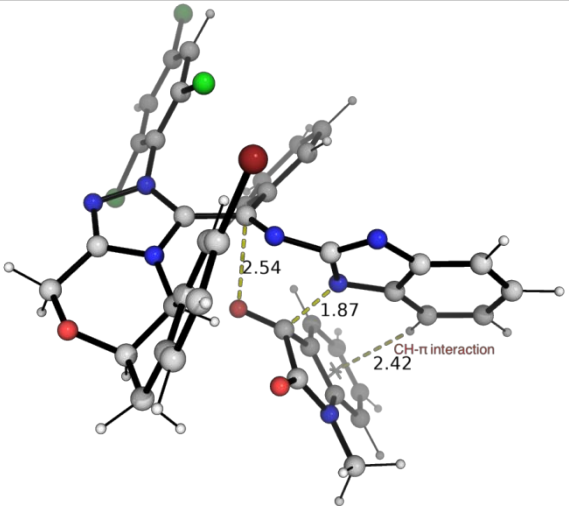	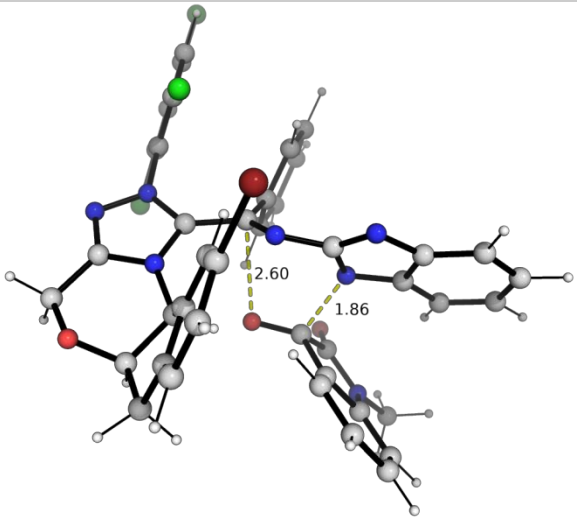
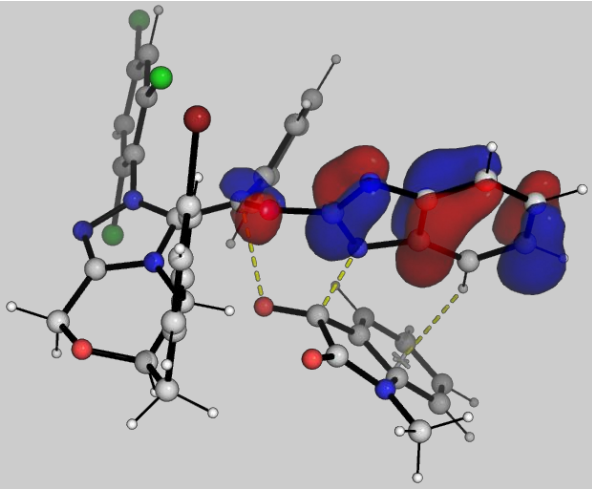	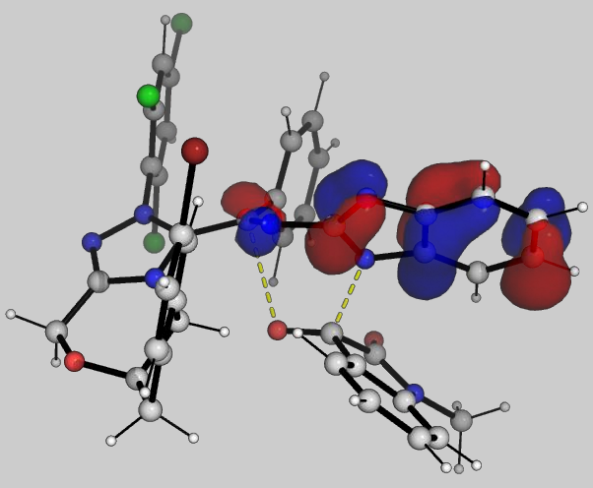

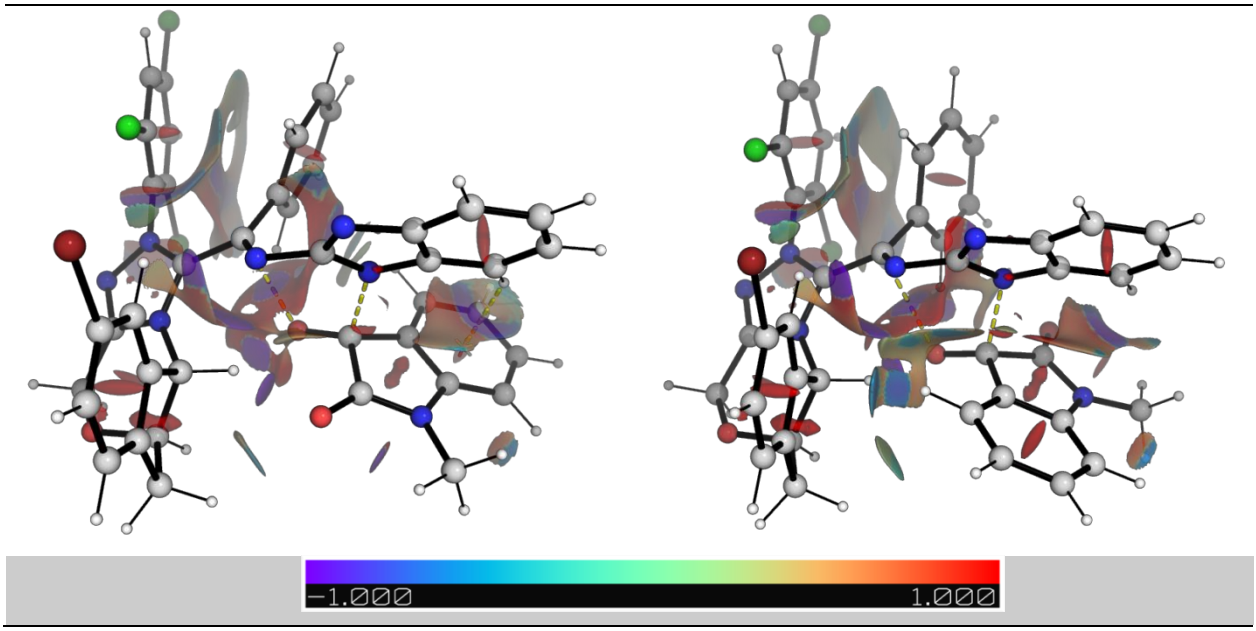

Figure S-5. Optimized TS structures, their HOMO (isosurface value = 0.05 au) and NCI plots. Key bond distances are given in Å.

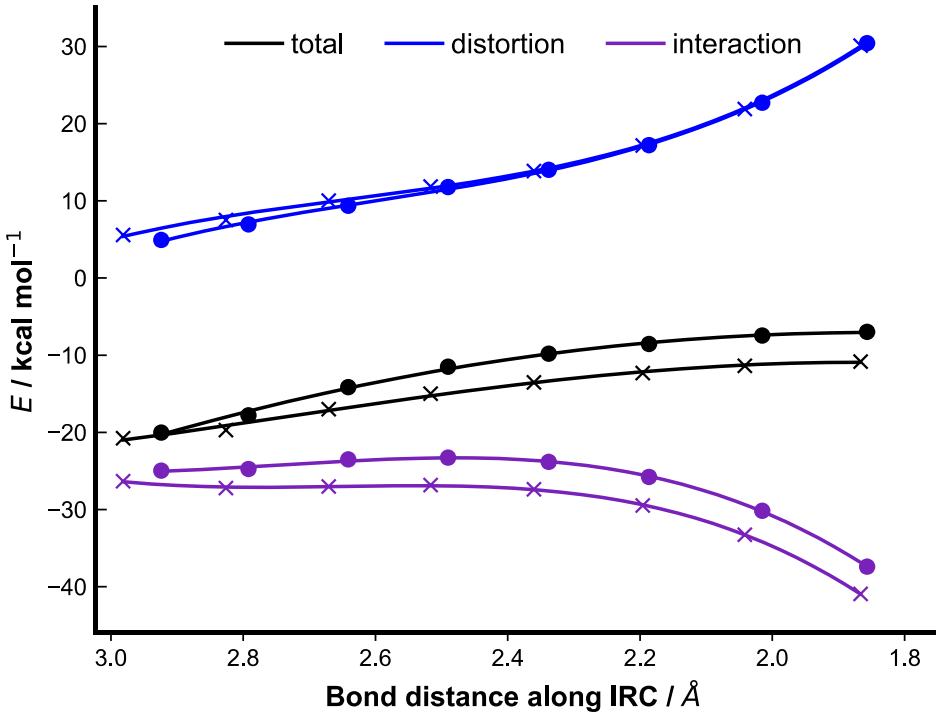

Figure S-6. The activation strain or distortion-interaction analyses applied to the IRC paths along the rate-determining transition state for the addition to the *Si*-face (*Si*-**TS-1**; cross markers) and the *Re*-face (*Re*-**TS-1**; full circle markers) of isatin substrate **2b**. All energies are calculated at M06-2X/def2TZVPP in gas-phase and used without any further corrections.

Other optimized structures

***Si*-V**	***Re*-V**
ΔG = 7.3 kcal mol^{-1}	ΔG = 8.9 kcal mol^{-1}
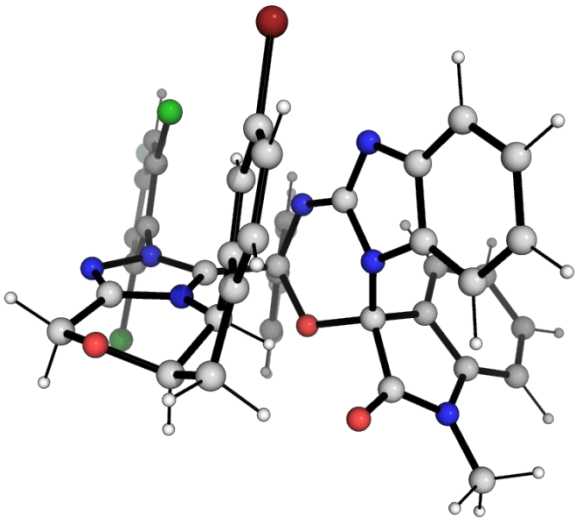	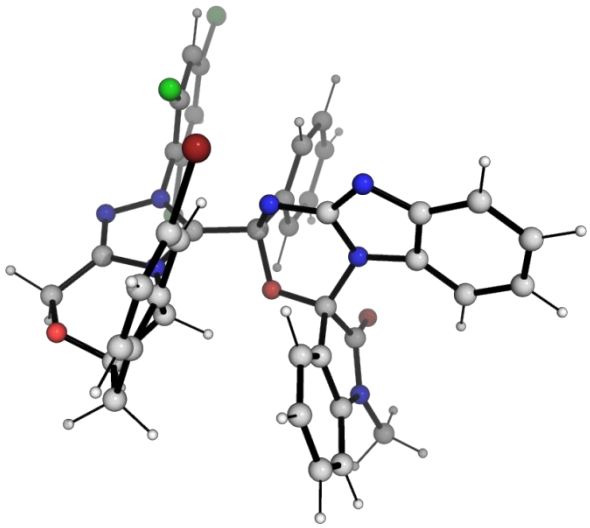
***Si*-TS-3**	***Re*- TS-3**
ΔG‡ = 15.7 kcal mol^{-1}	ΔG‡ = 15.6 kcal mol^{-1}
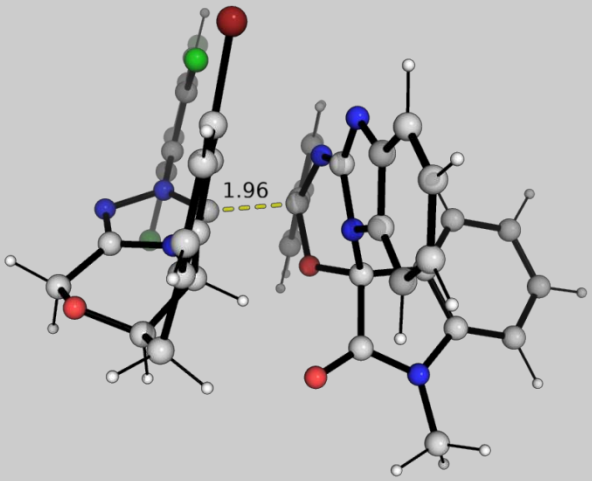	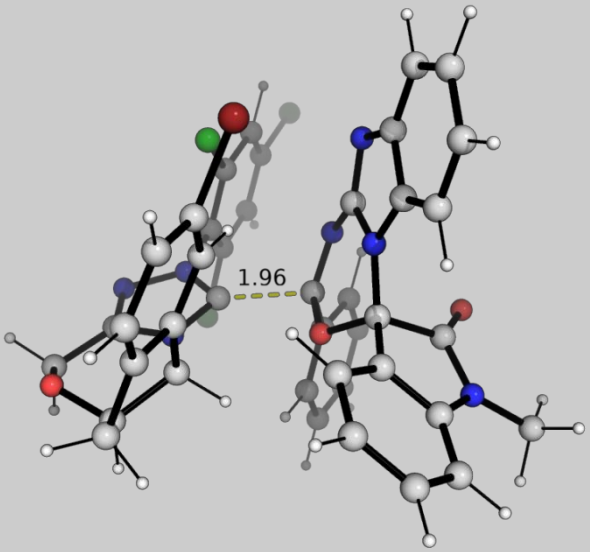
***Si*-NHC D···3b complex**	*Re*-NHC **D···3b** complex
ΔG‡ = -1.9 kcal mol^{-1}	ΔG‡ = -2.5 kcal mol^{-1}

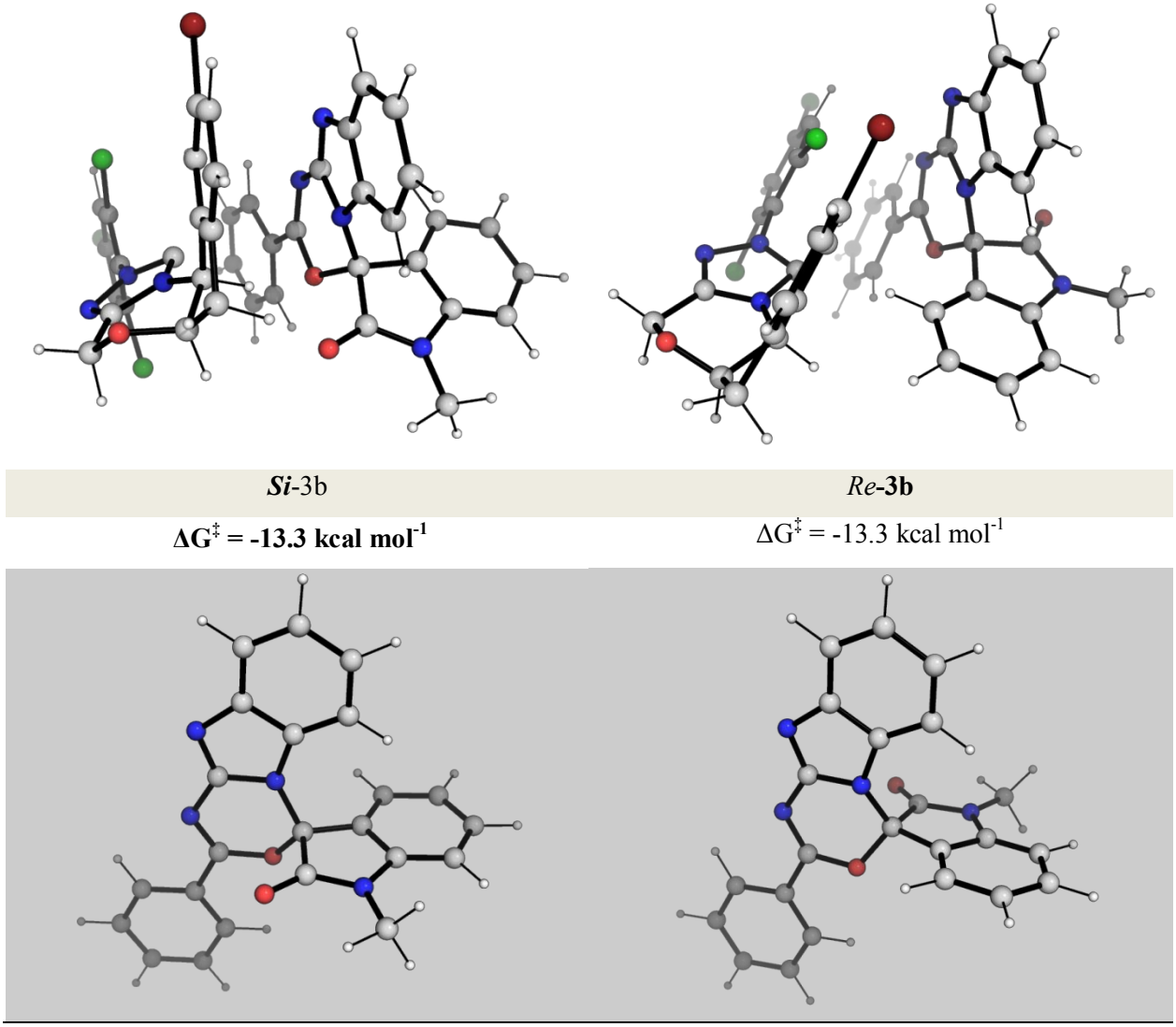

***Si*-3b**	***Re*-3b**
$\Delta G^{\ddagger}$ = -13.3 kcal mol^{-1}	$\Delta G^{\ddagger}$ = -13.3 kcal mol^{-1}

Figure S-7. Optimized structures and their associated Gibbs energies for the reaction between intermediate **III-3b** and isatin substrate **2b**. Key bond distances are given in Å.

Relaxed potential energy surface (PES) scan for concerted, synchronous TSs

Figure S-8 shows the 2-D relaxed PES scans along the two key bonds (C–N and C–O) for the addition of intermediate **III-3b** to isatin **2b**. We see that for addition to either the *Si*-face (Figure S-6a) or the *Re*-face (Figure S-6b), no concerted, synchronous TS structure is possible since no first-order saddle point can be found in this region.

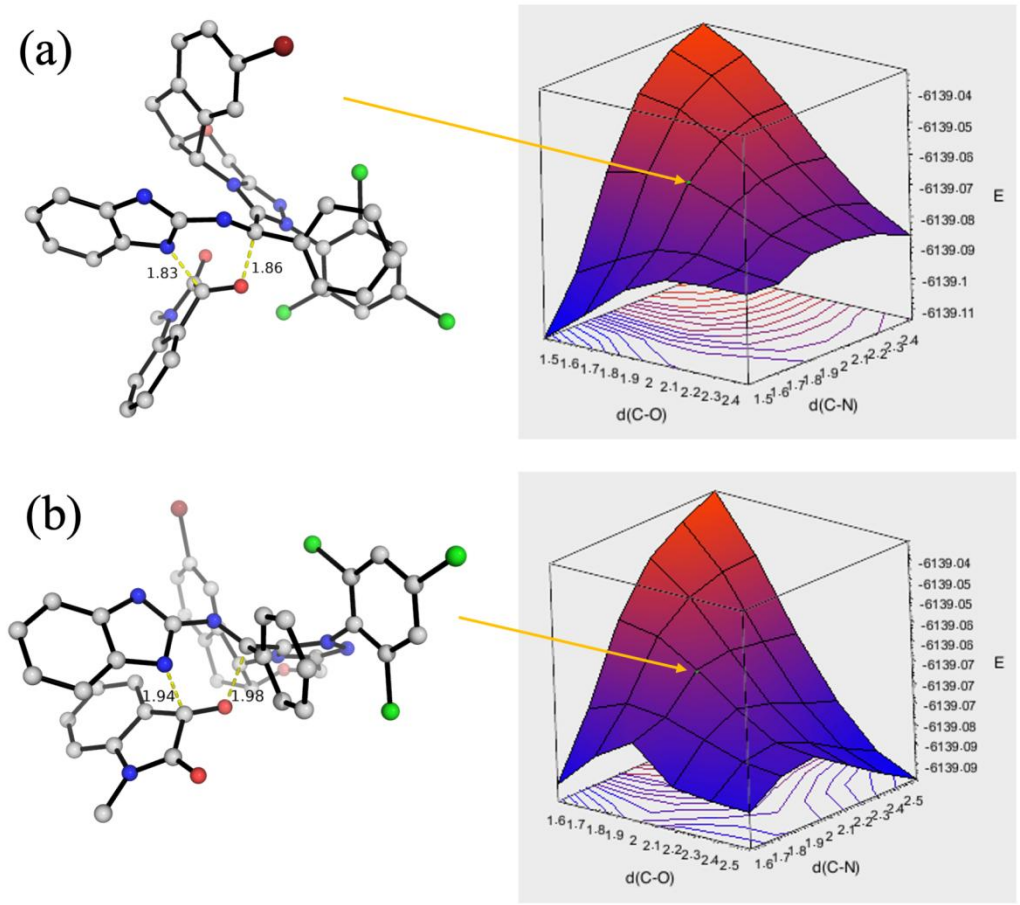

Figure S-8. Two-dimensional relaxed PES scans for formal [4+2] cycloaddition from (a) Si-face and (b) Re-face of the isatin substrate **2b**.

Reaction between III-3ac and 2b

Figure S-9 shows the stereo-determining TS structures for the reaction between intermediate **III-3ac** and isatin substrate **2b** which yield the product **3ac**. The reaction mechanisms are expected to be the same as discussed previously, i.e., the reaction proceeds via a concerted, highly asynchronous mechanism. The bond lengths in these TSs again support such a mechanism: the C–N bond formation occurs at 1.88Å (*Si*-**TS-1-3ac**) and 1.86Å (*Re*-**TS-1-3ac**), while the C–O bonds are much longer at 2.57Å (*Si*-**TS-1-3ac**) and 2.62 Å (*Si*-**TS-1-3ac**).

The reaction barriers in this case (20.3 and 23.0 kcal mol^{-1}) are higher than that between **III-3b** and **2b** (16.1 and 18.7 kcal mol^{-1}). The lack of a Ph-ring in intermediate **III-3ac** could result in less favorable interaction in this case than in **III-3b**, resulting in higher activation barriers. These computational results are consistent

with experimental finding that the functionalization of imine **1ac** gives a lower yield (52%; reactants recovered) than of imine **1a** (97%).

***Si*-TS-1-3ac**	***Re*-TS-1-3ac**
$\Delta G^{\ddagger}$ = 20.3 kcal mol^{-1}	$\Delta G^{\ddagger}$ = 23.0 kcal mol^{-1}
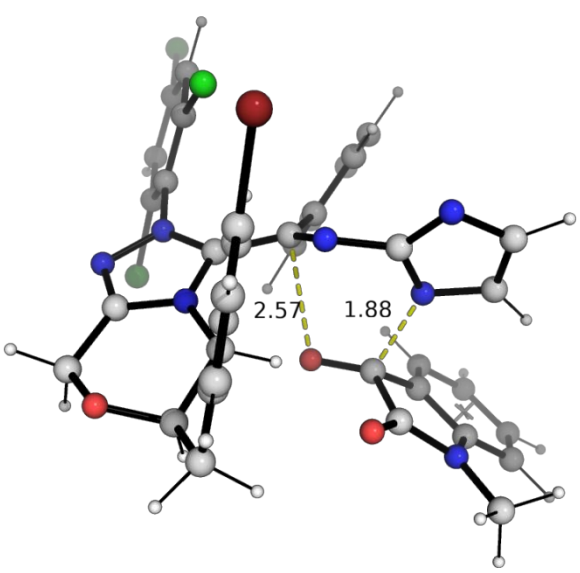	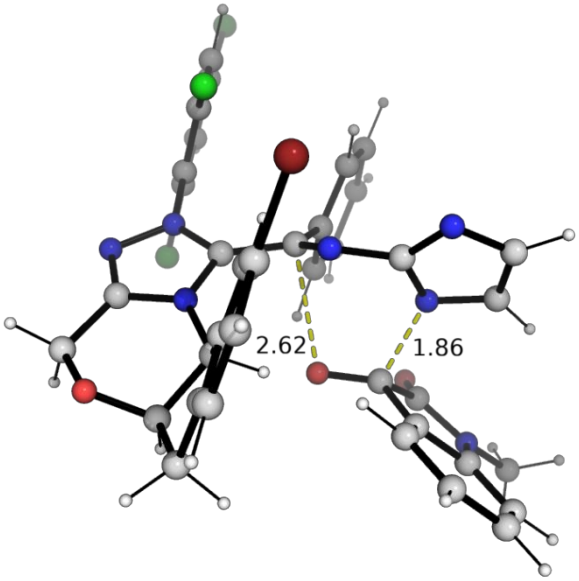
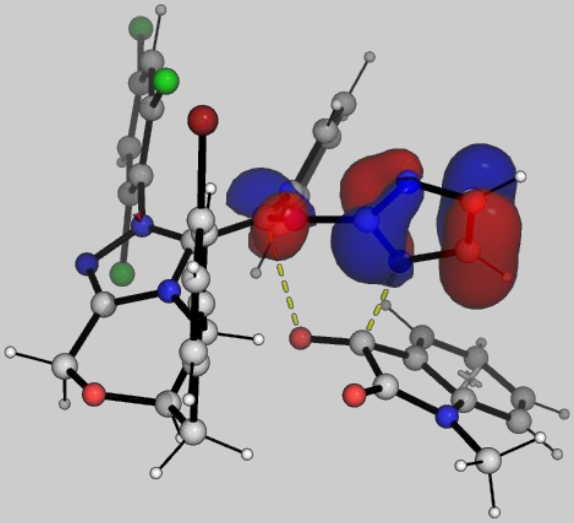	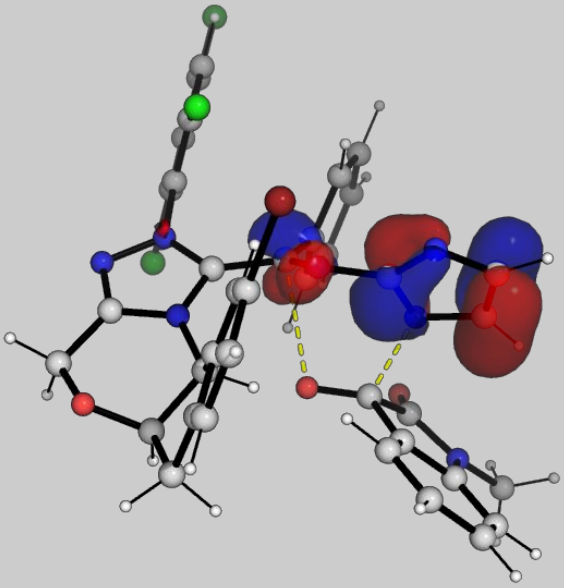

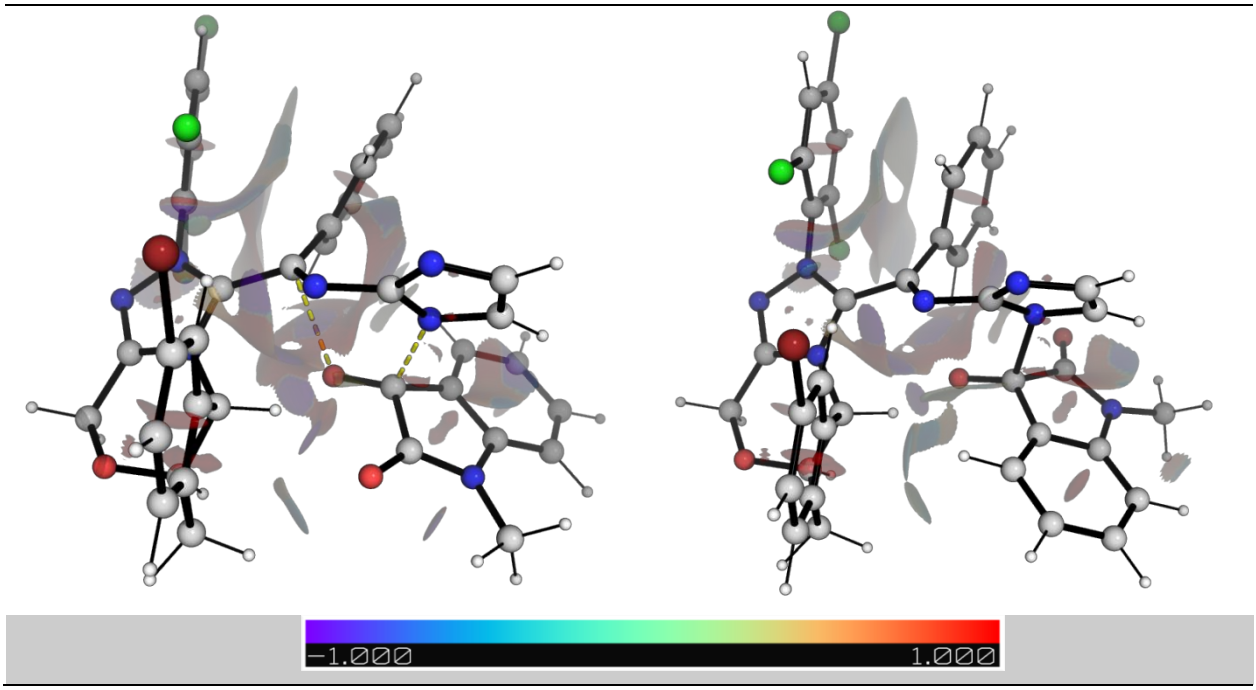

Figure S-9. Optimized TS structures, their HOMO (isosurface value = 0.05 au) and NCI plots for the stereo-determining TSs for the reaction between intermediate **III-3ac** and isatin substrate **2b**. Key bond distances are given in Å.

Optimized structures and absolute energies, zero-point energies

Geometries of all optimized structures (in .xyz format with their associated energy in Hartrees) are included in a separate folder named *xyz_structures* with an associated readme.txt file. All these data have been deposited with this Supporting Information and uploaded to zenodo.org (DOI: 10.5281/zenodo.4314003)

Absolute values (in Hartrees) for SCF energy, zero-point vibrational energy (ZPE), enthalpy and quasi-harmonic Gibbs free energy (at 298.15K) for gas-phase M06-2X/def2-SVP optimized structures are given below. Single point corrections in SMD dichloromethane using M06-2X/def2-TZVP functional are also included.

Structure	E/au	ZPE/au	H/au	T.S/au	G/au	qh-G/au	SP M06-2X/def2TZVP SMD(DCM)
III-3b	-5587.312242	0.464136	-5586.8134	0.101504	-5586.91492	-5586.906214	-5589.941105
IV-3b-c2	-5587.311914	0.464124	-5586.8131	0.100965	-5586.9141	-5586.90566	-5589.940207
IV-3b-c3	-5587.306555	0.464074	-5586.8076	0.102918	-5586.9105	-5586.900991	-5589.938955
2b	-551.748147	0.145384	-551.59238	0.042136	-551.634513	-551.634343	-552.3856815
nhc-c1	-4884.928065	0.261136	-4884.645	0.073281	-4884.71831	-4884.713313	-4886.769456
nhc-c2	-4884.928065	0.261136	-4884.645	0.073275	-4884.7183	-4884.71331	-4886.769457
Re-III···2b **complex**	-6139.099679	0.610953	-6138.4431	0.124072	-6138.56714	-6138.556405	-6142.341829
Re-TS-1	-6139.078147	0.611245	-6138.4224	0.121203	-6138.54356	-6138.533208	-6142.322033
Re-V	-6139.099611	0.6139	-6138.4417	0.120293	-6138.56195	-6138.551547	-6142.340797
Re-TS-3	-6139.095546	0.612517	-6138.4392	0.118402	-6138.55763	-6138.548074	-6142.329441
Re-**NHC** D···3b **complex**	-6139.120655	0.613393	-6138.4624	0.121885	-6138.58427	-6138.573711	-6142.357847
Re-3b	-1254.16056	0.351129	-1253.7871	0.070949	-1253.85801	-1253.854073	-1255.579983
Si-III···2b **complex**	-6139.101277	0.611123	-6138.4446	0.124585	-6138.56914	-6138.557948	-6142.341445
Si-TS-1	-6139.084959	0.611625	-6138.4288	0.121544	-6138.55035	-6138.539837	-6142.326383
Si-V	-6139.111298	0.614299	-6138.4531	0.118865	-6138.57195	-6138.562344	-6142.344314
Si-TS-3	-6139.101713	0.613099	-6138.4449	0.118294	-6138.56323	-6138.553672	-6142.330108
Si-**NHC** D···3b **complex**	-6139.123981	0.613515	-6138.4656	0.122744	-6138.58834	-6138.577371	-6142.356659

Si-3b	-1254.16056	0.351129	-1253.7871	0.070949	-1253.85801	-1253.854073	-1255.579983
III-3ac	-5433.848206	0.41673	-5433.3994	0.095036	-5433.49441	-5433.487015	-5436.302217
Si-TS-2-3ac	-5985.606936	0.563785	-5985.0011	0.115971	-5985.1171	-5985.107405	-5988.68005
Re-TS-2-3ac	-5985.599639	0.563537	-5984.994	0.11628	-5985.11031	-5985.100509	-5988.675442

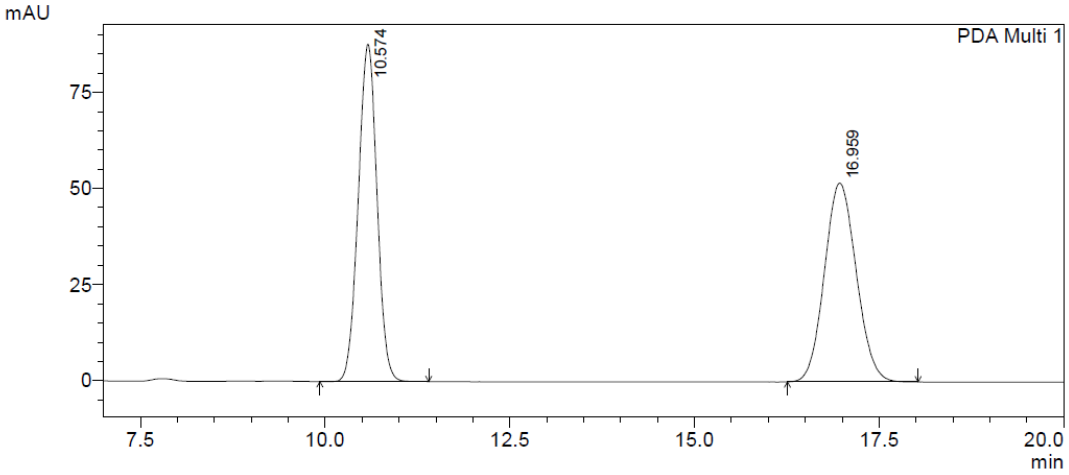

Peak#	Ret. Time	Area	Height	Area %	Height %
1	10.574	1550560	87761	49.967	62.937
2	16.959	1552608	51682	50.033	37.063
Total		3103169	139443	100.000	100.000

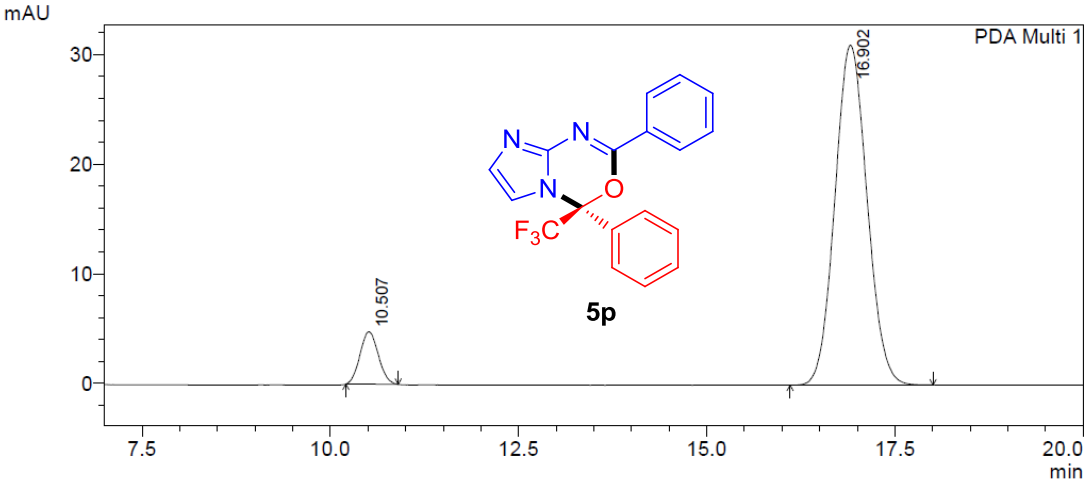

5p

PDA Ch1 254nm 4nm

Peak#	Ret. Time	Area	Height	Area %	Height %
1	10.507	80846	4769	8.063	13.328
2	16.902	921835	31016	91.937	86.672
Total		1002681	35785	100.000	100.000

References

[1] a) Wang, G.; Fu, Z.; Huang, W. Access to Amide from Aldimine via Aerobic Oxidative Carbene Catalysis and LiCl as Cooperative Lewis Acid. *Org. Lett.* **2017**, *19*, 3362-3365; b) Vashist, N.; Sambi, S. S.; Narasimhan, B.; Kumar, S.; Lim, S. M.; Shah, S.; Ramasamy, K.; Mani, V. Synthesis and Biological Profile of Substituted Benzimidazoles. *Chemistry Central Journal* **2018**, *12*, 125; c) Li, H.; Zhao, J.; Zeng, L.; Hu, W. Organocatalytic Asymmetric Domino Aza-MichaelMannich Reaction:

Synthesis of Tetrahydroimidazopyrimidine Derivatives. *J. Org. Chem.* **2011**, *76,* 8064-8069.

Full reference for Gaussian software:

Gaussian 16, Revision A.01, Frisch, M. J.; Trucks, G. W.; Schlegel, H. B.; Scuseria, G. E.; Robb, M. A.; Cheeseman, J. R.; Scalmani, G.; Barone, V.; Mennucci, B.; Petersson, G. A.; Nakatsuji, H.; Caricato, M.; Li, X.; Hratchian, H. P.; Izmaylov, A. F.; Bloino, J.; Zheng, G.; Sonnenberg, J. L.; Hada, M.; Ehara, M.; Toyota, K.; Fukuda, R.; Hasegawa, J.; Ishida, M.; Nakajima, T.; Honda, Y.; Kitao, O.; Nakai, H.; Vreven, T.; Montgomery Jr., J. A.; Peralta, J. E.; Ogliaro, F.; Bearpark, M.; Heyd, J. J.; Brothers, E.; Kudin, K. N.; Staroverov, V. N.; Kobayashi, R.; Normand, J.; Raghavachari, K.; Rendell, A.; Burant, J. C.; Iyengar, S. S.; Tomasi, J.; Cossi, M.; Rega, N.; Millam, J. M.; Klene, M.; Knox, J. E.; Cross, J. B.; Bakken, V.; Adamo, C.; Jaramillo, J.; Gomperts, R.; Stratmann, R. E.; Yazyev, O.; Austin, A. J.; Cammi, R.; Pomelli, C.; Ochterski, J. W.; Martin, R. L.; Morokuma, K.; Zakrzewski, V. G.; Voth, G. A.; Salvador, P.; Dannenberg, J. J.; Dapprich, S.; Daniels, A. D.; Farkas, Ö.; Foresman, J. B.; Ortiz, J. V; Cioslowski, J.; Fox, D. J. Gaussian, Inc., Wallingford CT, 2016.

[2] Grimme, S.; Bannwarth, C.; Shushkov, P. A Robust and Accurate Tight-Binding Quantum Chemical Method for Structures, Vibrational Frequencies, and Noncovalent Interactions of Large Molecular Systems Parametrized for All Spd-Block Elements (Z = 1-86). J. Chem. Theory Comput. 2017, 13 (5), 1989–2009. https://doi.org/10.1021/acs.jctc.7b00118.

[3] Manby, F. R.; Miller, T. F.; Bygrave, P. J.; Ding, F.; Dresselhaus, T.; Buccheri, A.; Bungey, C.; Lee, S. J. R.; Meli, R.; Steinmann, C.; et al. Entos : A Quantum Molecular Simulation Package. ChemRxiv. 2019. https://doi.org/10.26434/chemrxiv.7762646.v2.

[4] Zhao, Y.; Truhlar, D. G. The M06 Suite of Density Functionals for Main Group Thermochemistry, Thermochemical Kinetics, Noncovalent Interactions, Excited States, and Transition Elements: Two New Functionals and Systematic Testing of Four M06-Class Functionals and 12 Other Function. Theor. Chem. Acc. 2008, 120 (1), 215–241. https://doi.org/10.1007/s00214-007-0310-x.

[5] Weigend, F.; Ahlrichs, R. Balanced Basis Sets of Split Valence, Triple Zeta Valence and Quadruple Zeta Valence Quality for H to Rn: Design and

Assessment of Accuracy. *Phys. Chem. Chem. Phys.* **2005**, *7*, 3297–3305. https://doi.org/10.1039/b508541a.

[6] Weigend, F. Accurate Coulomb-Fitting Basis Sets for H to Rn. *Phys. Chem. Chem. Phys.* **2006**, *8*, 1057–1065. https://doi.org/10.1039/B515623H.

[7] Frisch, M. J.; Trucks, G. W.; Schlegel, H. B.; Scuseria, G. E.; Robb, M. A.; Cheeseman, J. R.; Scalmani, G.; Barone, V.; Mennucci, B.; Petersson, G. A.; et al. Gaussian 16, Revision A.01. 2016.

[8] Fukui, K. Formulation of the Reaction Coordinate. *J. Phys. Chem.* **2005**, *74*, 4161–4163. https://doi.org/10.1021/j100717a029.

[9] Fukui, K. The Path of Chemical Reactions - The IRC Approach. *Acc. Chem. Res.* **1981**, *14*, 363–368. https://doi.org/10.1021/ar00072a001.

[10] Marenich, A. V.; Cramer, C. J.; Truhlar, D. G. Universal Solvation Model Based on Solute Electron Density and on a Continuum Model of the Solvent Defined by the Bulk Dielectric Constant and Atomic Surface Tensions. *J. Phys. Chem. B* **2009**, *113*, 6378–6396. https://doi.org/10.1021/jp810292n.

[11] Grimme, S. Supramolecular Binding Thermodynamics by Dispersion-Corrected Density Functional Theory. *Chem.: Eur. J.* **2012**, *18*, 9955–9964. https://doi.org/10.1002/chem.201200497.

[12] Funes-Ardoiz, I.; Paton, R. S. GoodVibes v1.0.1 http://doi.org/10.5281/zenodo.56091. https://doi.org/10.5281/zenodo.56091.

[13] Contreras-García, J.; Johnson, E. R.; Keinan, S.; Chaudret, R.; Piquemal, J. P.; Beratan, D. N.; Yang, W. NCIPLOT: A Program for Plotting Noncovalent Interaction Regions. *J. Chem. Theory Comput.* **2011**, *7*, 625–632. https://doi.org/10.1021/ct100641a.

[14] Sosa, C.; Andzelm, J.; Elkin, B. C.; Wimmer, E.; Dobbs, K. D.; Dixon, D. A. A Local Density Functional Study of the Structure and Vibrational Frequencies of Molecular Transition-Metal Compounds. *J. Phys. Chem.* **1992**, *96*, 6630–6636. https://doi.org/10.1021/j100195a022.

[15] Godbout, N.; Salahub, D. R.; Andzelm, J.; Wimmer, E. Optimization of Gaussian-Type Basis Sets for Local Spin Density Functional Calculations. Part I. Boron through Neon, Optimization Technique and Validation. *Can. J. Chem.* **1992**, *70*, 560–571. https://doi.org/10.1139/v92-079.

[16] Schrödinger, L. *The PyMOL Molecular Graphics Development Component,*

Version 1.8; 2015.

[17] Ess, D. H.; Houk, K. N. Distortion/Interaction Energy Control of 1,3-Dipolar Cycloaddition Reactivity. *J. Am. Chem. Soc.* **2007**, *129*, 10646–10647. https://doi.org/10.1021/ja0734086.

[18] Bickelhaupt, F. M.; Houk, K. N. Analyzing Reaction Rates with the Distortion/Interaction-Activation Strain Model. *Angew. Chem. Int. Ed.* **2017**, *56*, 10070–10086. https://doi.org/10.1002/anie.201701486.

[19] Bickelhaupt, F. M. Understanding Reactivity with Kohn-Sham Molecular Orbital Theory: E2-SN2 Mechanistic Spectrum and Other Concepts. *J. Comput. Chem.* **1999**, *20*, 114–128. https://doi.org/10.1002/(SICI)1096-987X(19990115)20:1<114::AID-JCC12>3.0.CO;2-L.

[20] Fernández, I.; Bickelhaupt, F. M. The Activation Strain Model and Molecular Orbital Theory: Understanding and Designing Chemical Reactions. *Chem. Soc. Rev.* **2014**, *43*, 4953–4967. https://doi.org/10.1039/c4cs00055b.

[21] Wolters, L. P.; Bickelhaupt, F. M. The Activation Strain Model and Molecular Orbital Theory. *Wiley Interdiscip. Rev. Comput. Mol. Sci.* **2015**, *5*, 324–343. https://doi.org/10.1002/wcms.1221.

[22] Vermeeren, P.; van der Lubbe, S. C. C.; Fonseca Guerra, C.; Bickelhaupt, F. M.; Hamlin, T. A. Understanding Chemical Reactivity Using the Activation Strain Model. *Nat. Protoc.* **2020**, *15*, 649–667. https://doi.org/10.1038/s41596-019-0265-0.

[23] Brethomé, A. V.; Fletcher, S. P.; Paton, R. S. Conformational Effects on Physical-Organic Descriptors: The Case of Sterimol Steric Parameters. *ACS Catal.* **2019**, *9*, 2313–2323. https://doi.org/10.1021/acscatal.8b04043.